Solvent Engineering for High-Performance Two-Dimensional Ruddlesden-Popper CsPbI$_3$ Solar Cells

Chen, Haiqiang ; Lei, Yutian ; Yao, Huanhuan; Li, Zhizai; Peng, Guoqiang ; Zhou, Xufeng ; Wang, Haoxu; Wang, Qian; Jin, Zhiwen

Citation (APA)
Chen, H., Lei, Y., Yao, H., Li, Z., Peng, G., Zhou, X., Wang, H., Wang, Q., & Jin, Z. (2022). Solvent Engineering for High-Performance Two-Dimensional Ruddlesden-Popper CsPbI$_3$ Solar Cells. *ACS Applied Energy Materials*, *5*(9), 11807-11814. https://doi.org/10.1021/acsaem.2c02345

Important note
To cite this publication, please use the final published version (if applicable).
Please check the document version above.

Solvent Engineering for High-Performance Two-Dimensional Ruddlesden−Popper CsPbI$_3$ Solar Cells

Haiqiang Chen, Yutian Lei, Huanhuan Yao, Zhizai Li, Guoqiang Peng, Xufeng Zhou, Haoxu Wang, Qian Wang,* and Zhiwen Jin

Cite This: https://doi.org/10.1021/acsaem.2c02345

Read Online

ACCESS | Metrics & More | Article Recommendations | Supporting Information

ABSTRACT: Two-dimensional (2D) Ruddlesden−Popper (RP) CsPbI$_3$ exhibits enhanced phase stability compared with 3D CsPbI$_3$. However, the issue of the uncontrollable crystallization process limits its photovoltaic performance. Here, the influence of a binary mixed solvent on the film quality and photovoltaic properties of (PEA)$_2$Cs$_4$Pb$_5$I$_{16}$ (n = 5) is studied in detail. It is demonstrated that the crystallization rate and crystal growth can be controlled by adjusting the amount of dimethyl sulfoxide (DMSO). Optimizing the solvent composition with adding 10% DMSO in pure dimethyl formamide (DMF) leads to perfect coverage, larger flaky 2D grains, reduced grain boundaries, and a better vertical orientation to the substrate due to the formation of a more stable intermediate phase. This can form good interface contact, which is beneficial to charge transport/extraction between TiO$_2$ (electron transport layer, ETL) and perovskite, finally resulting in improved device performance. The enhancement of the power conversion efficiency of the optimized device based on DMF/DMSO (9:1) is 3.57% compared with the reference device based on pure DMF. This work illustrates the role of crystallization kinetics in the RP CsPbI$_3$ film and offers a simple and effective method for high-performance 2D CsPbI$_3$ solar cells.

KEYWORDS: 2D inorganic perovskites, Ruddlesden−Popper phase, solvent engineering, crystallization kinetics, intermediate phase
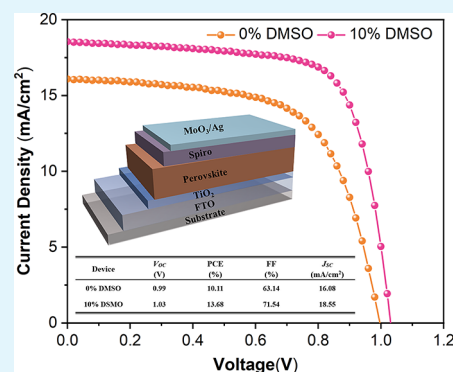
INTRODUCTION

Cesium lead halide perovskites without volatile organic compositions, whose general chemical formula is CsPbX$_3$ (X is halides or their mixture), have attracted wide attention due to excellent thermal stability and high formation energy.[1−5] Among them, CsPbI$_3$ with a desirable band gap (<1.73 eV) and good stability shows great potential in the photovoltaic field.[6−9] So far, the power conversion efficiency (PCE) of CsPbI$_3$-based perovskite solar cells (PSCs) improved to 21.0% from the first reported 2.9% in 2015.[10,11] However, the poor phase stability is a huge obstacle to further commercial application.[12] Desirable photoactive black-phase perovskite (γ-CsPbI$_3$) can spontaneously transform to undesirable yellow-phase nonperovskite (δ-CsPbI$_3$) caused by a low limit of tolerance factor of 0.81 (0.8 < τ < 1.0) at room temperature (RT).[13,14] Many strategies have been used to enhance the phase stability of black-phase CsPbI$_3$ perovskite, for example, ionic incorporation, organic cation surface termination, reduced dimensions (quantum dot, quasi two-dimensional (2D)), and so on.[15−20] Among these strategies, 2D or quasi-2D CsPbI$_3$ is an extremely effective and promising one.

2D perovskites can be classified into three types, namely, the ⟨100⟩-, ⟨110⟩-, and ⟨111⟩-oriented perovskites with different connection modes (corner-sharing, edge-sharing, and face-sharing) of [PbI$_6$]$^{4-}$ octahedrons.[21] Among them, the ⟨100⟩-

oriented 2D perovskites have attracted wide attention. It can be divided into four types according to different kinds of organic spacer cations at A sites, namely, the Ruddlesden−Popper (RP) phase, the Dion−Jacobson (DJ) phase, the alternating cation (ACI) phase, and the Aurivillius phase.[22−27] The Aurivillius phase and the ACI phase adopt the general formulas (Bi$_2$O$_2$)(A$_{n-1}$B$_n$X$_{3n+1}$) and (GA)A$_n$B$_n$X$_{3n+1}$ (GA$^+$ = guanidinium), respectively. The RP phase and DJ phase perovskites have the chemical formula A′$_m$A$_{n-1}$B$_n$X$_{3n+1}$, for the RP phase, where A′ represents a large monovalent organic cation (m = 2), such as butylammonium(BA$^+$) or phenyl-ethylammonium (PEA$^+$), while for the DJ phase, A′ represents a divalent organic cation (m = 1), such as 3-(aminomethyl)-piperidinium (3AMP^{2+}) or 1,4-butanediamine (BDA^{2+}).[22,28−30] Moreover, n denotes the number of inorganic [PbI$_6$]$^{4-}$ octahedral layers.[31] In addition to the hydrophobicity of bulky organic cations and improved stability due to stronger van der Waals forces between capping organic cations and

[PbI$_6$]$^{4-}$ octahedrons, 2D perovskites also show tunability of optoelectronic properties.[32,33] However, in contrast to their 3D counterparts, 2D-based PSCs are relatively inferior, which is caused by many factors, such as their huge exciton binding energy, low absorption coefficient, and inferior charge transporting capability.[34] Among these factors, the charge transporting capability is closely related to the surface/interface morphology.

Plenty of efforts, including controlling the crystallization process, altering the phase orientation, etc., are dedicated to improve the PCE of 2D PSCs.[32] Solvent composition adjustment has been successfully used to modulate the crystallization process and enhance device performance. For example, Qiu et al. showed how the processing solvents affect the crystallization kinetics, phase distribution, and crystal growth orientation of the BA$_2$MA$_3$Pb$_4$I$_{13}$-based perovskite film fabricated by hot-casting and found that dimethylacetamide (DMAC) can effectively facilitate rapid crystallization of 2D RP perovskite, resulting in a high-quality BA$_2$MA$_3$Pb$_4$I$_{13}$ film with an increased photoluminescence (PL) intensity and carrier lifetime. Finally, DMAC-based devices exhibit the best PCE of 12.15%.[35] Gao et al. observed that (PEA)$_2$MA$_4$Pb$_5$I$_{16}$-based RP perovskite films grow along with a vertical orientation to the substrate surface and exhibit much improved optoelectronic properties by optimizing the solvent composition, and finally, the PCE of the device significantly increased from 6.78 to 12.29%.[34] After adding a proper amount of DMSO to DMF, the morphology and crystallinity of the (GA)MA$_5$Pb$_5$I$_{16}$ perovskite film are improved with more distributed preferential quantum wells. Finally, the device realized a high PCE of 19.18%.[36] Although solvent engineering has been successfully used to manipulate the crystallization process of low-dimensional organic—inorganic hybrid perovskite films, the effect of solvent engineering on film quality and device performance of 2D CsPbI$_3$ remains ambiguous.

Herein, the solvent effects on the 2D RP CsPbI$_3$ film quality and photovoltaic properties are studied in detail. It exhibits that the different coordination ability between diverse solvent systems and the 2D CsPbI$_3$ precursor can significantly affect the evolution of the intermediate phase and the perovskite phase. The more stable intermediate phase and the retarded crystallization process are observed in the binary solvent system. Finally, a high-quality 2D RP CsPbI$_3$ film is obtained with the binary mixed solvent of DMF/DMSO (9:1), and the corresponding PSCs show significant efficiency improvement from 10.11 to 13.68%.

■ RESULTS AND DISCUSSION

To study the effect of solvent engineering on crystallization kinetics, film quality, and device photovoltaic properties, the different solvents containing pure DMF (0% DMSO) and DMF/DMSO mixed solvents with different amounts of DMSO (5, 10, and 20% DMSO) are used to prepare 2D RP (PEA)$_2$(Cs)$_4$Pb$_5$I$_{16}$ films. The surface morphologies of the films are measured using scanning electron microscopy (SEM), as shown in Figure 1. For the reference film (0% DMSO), incomplete coverage with oversized pinholes (≈1 μm) and an underlying TiO$_2$ layer are obviously observed, indicating a poor morphology. After adding 5% DMSO to the pure DMF solvent, the film exhibits smaller pinholes and density-enhanced grains. However, simultaneously, grain boundaries are also obvious. Further increasing the amount of DMSO to 10%, smooth and compact films with larger, more homoge-
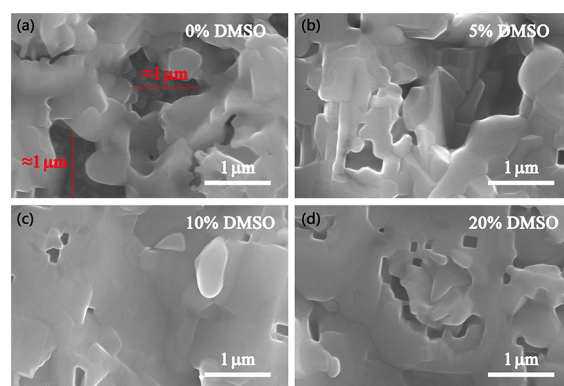

Figure 1. SEM images of the (PEA)$_2$Cs$_4$Pb$_5$I$_{16}$ films: (a) 0% DMSO, (b) 5% DMSO, (c) 10% DMSO, and (d) 20% DMSO.

neous 2D flaky grains and fine coverage are observed. However, pinholes in the film will deteriorate again when the amount of DMSO is increased to 20%. Therefore, the optimal film is obtained with 10% DMSO in the solvent.

The incomplete coverage and grain boundaries will result in inferior charge transport pathways and facile charge carrier recombination.[37] Hence, improving the film surface coverage with larger and more compact 2D flaky grains is beneficial to enhancing device performance.[38−41] Atomic force microscopy (AFM) images further exhibit the improved surface morphology of the (PEA)$_2$(Cs)$_4$Pb$_5$I$_{16}$ film after dealing with 10% DMSO, as shown in Figure S1a. The root-mean-square roughness (RMS) value of the reference film is 268 nm; however, the optimized film with 10% DMSO only has the value of 198 nm. AFM results further suggest the improved uniformity after adding 10% DMSO, which is consistent with the above SEM results. Contact angle measurements were conducted to investigate the hydrophobicity of thin films, as shown in Figure S1b. The optimized film shows a larger value of 74.17° compared with the reference film (69.31°), implying better hydrophobicity, which is probably due to the compact connection of grains and reduced grain boundaries.

X-ray diffraction (XRD) patterns were used to investigate the influence of solvent composition on crystallinity. In Figure 2a, there are two quite sharp dominant diffraction peaks at 14.50 and 29.05° for all thin films, corresponding to the (111) and (202) lattice planes, respectively. Moreover, no additional diffraction peaks (below 10°) are observed, suggesting a vertical crystal orientation to the substrate surface, that is to say that inorganic [PbI$_6$]$^{4-}$ octahedral layers are perpendicular to the substrate.[42] The reference film exhibits weak diffraction intensities, and the intensities gradually enhance with increasing amounts of DMSO and reach a maximum value at 10% DMSO. However, the diffraction intensities will decrease when the amount of DMSO exceeds 10%, which is consistent with SEM and AFM results. The full-width at half-maximum (FWHM) values of the (111) and (202) lattice planes for all films as a function of different amounts of DMSO are plotted in Figure S2. Obviously, the optimized film exhibits a decreased FWHM value of 0.32 compared with the reference film (0.35), also indicating the increase of film crystallinity, which is beneficial to suppressing charge carrier recombination and improving charge carrier transport.[43] Meanwhile, decreased FWHM values also indicate a more vertical orientation.[36] Note that the (202) lattice plane orientation represents [PbI$_6$]$^{4-}$ octahedral layer growth in complete
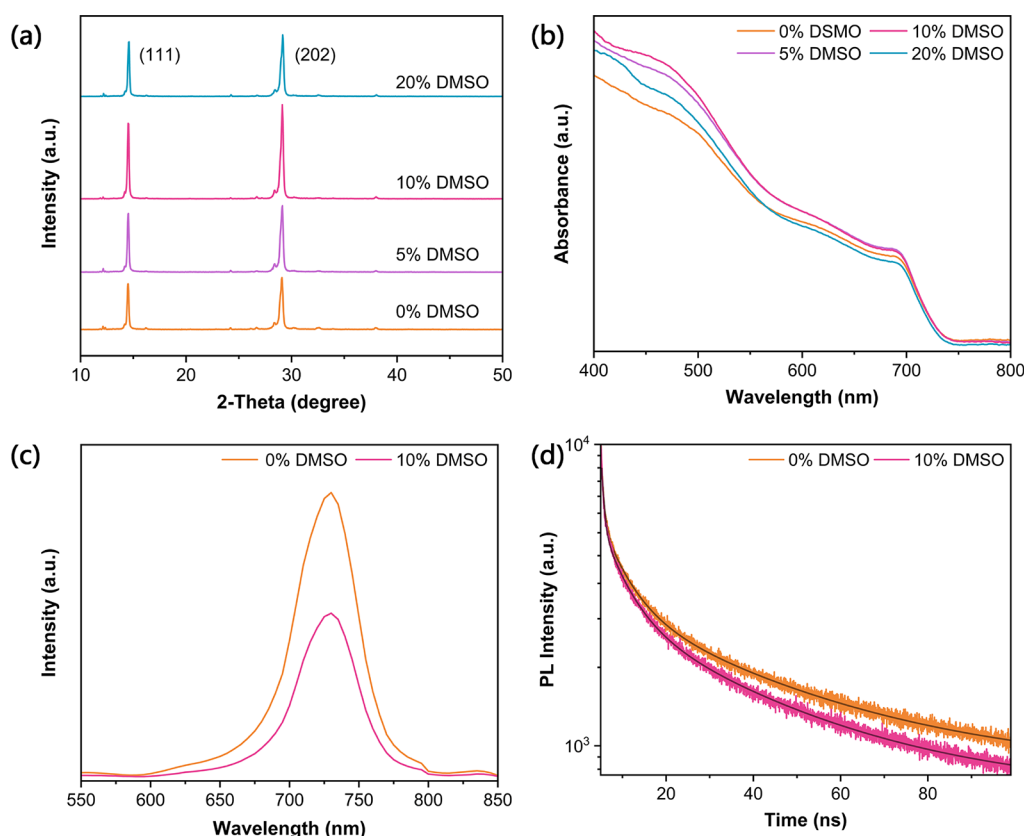
Figure 2. Optical characterization of the $(PEA)_2Cs_4Pb_5I_{16}$ films: (a) XRD patterns, (b) UV−vis absorption spectra, and (c,d) PL spectra and TRPL spectra of the reference and optimized $(PEA)_2Cs_4Pb_5I_{16}$ films on TiO_2/FTO substrates.

orthogonal alignment to the substrate, while the (111) lattice plane orientation can lead to a slanted vertical alignment.[44] For the reference and optimized films, two dominant diffraction peak intensity ratios of $I_{(202)}/I_{(111)}$ are summarized in Table S1. The optimized film exhibits an increased value of 1.24 compared with the reference film (1.13), again indicating the more vertical growth orientation for the optimized film.[23] XRD patterns for the reference and optimized $(PEA)_2Cs_4Pb_5I_{16}$ films under different annealing times are used to understand the effect of solvent properties on crystallization kinetics and structural evolution. Solvent properties of DMF and DMSO are summarized in Table S2. In Figure S3, the intermediate phases (diffraction peaks at 2θ of <10°) are observed in two films at annealing times of 2 and 4 min. In contrast, continuing annealing to 6 min, the intermediate phase can only be observed in the optimized film, suggesting a more stable intermediate phase due to the stronger polarity of DMSO. Compared with the optimized film, the reference film shows stronger diffraction peaks of perovskites at annealing times of 4 and 6 min.

The optical images of the reference and optimized $(PEA)_2Cs_4Pb_5I_{16}$ films under different annealing times are shown in Figure S4. Clearly, the reference film turns black more quickly than the optimized film, suggesting rapid crystallization of the reference film during the annealing process, which is consistent with the evolution results of XRD. The rapid crystallization of the reference film should be ascribed to the weak coordination ability of DMF with Pb^{2+} in precursor solution and a high evaporation rate. It is well-known that fast crystal nucleation and growth will form a lot of small grains and a large number of grain boundaries, leading to high

defect density.[45] For the optimized film, the more stable intermediate phase will retard nucleation and crystal growth, thus needing a longer time to form the final perovskite structure. From Figure S4, it can be observed that apparently, when the annealing time reaches 11 min, the optimized film still remains black, whereas the reference film has begun to decompose. The low nucleation rate allows that the crystal nuclei have enough time and space to grow into large grains, which could reduce nonradiative recombination.[46] Therefore, a slower nucleation rate is beneficial to improving the film quality.

The photophysical properties of $(PEA)_2(Cs)_4Pb_5I_{16}$ films are investigated using various spectroscopy techniques. The UV−vis absorption spectra of all films are shown in Figure 2b. As the amount of DMSO increasing from 0 to 10%, films exhibit a significantly enhanced absorption intensity between 400 and 750 nm, indicating the better light management ability of perovskite films. Further increasing the amount of DMSO to 20%, too much amounts of DMSO lead to reduced absorption intensity, which is highly consistent with SEM and XRD results. Steady-state photoluminescence (PL) measurements of the reference and optimized $(PEA)_2Cs_4Pb_5I_{16}$ films with the architecture of glass/FTO/compact-TiO_2/perovskite were carried out, as shown in Figure 2c. The optimized film exhibits the lower peak intensity, which suggests the more effective charge transport/extraction between TiO_2 and perovskite films due to improved surface coverage and good interface contact between TiO_2 and perovskite films.

Figure 2d displays the time-resolved PL (TRPL) spectra of the reference and optimized $(PEA)_2(Cs)_4Pb_5I_{16}$ films with the above architecture. The data are fitted with a triple exponential

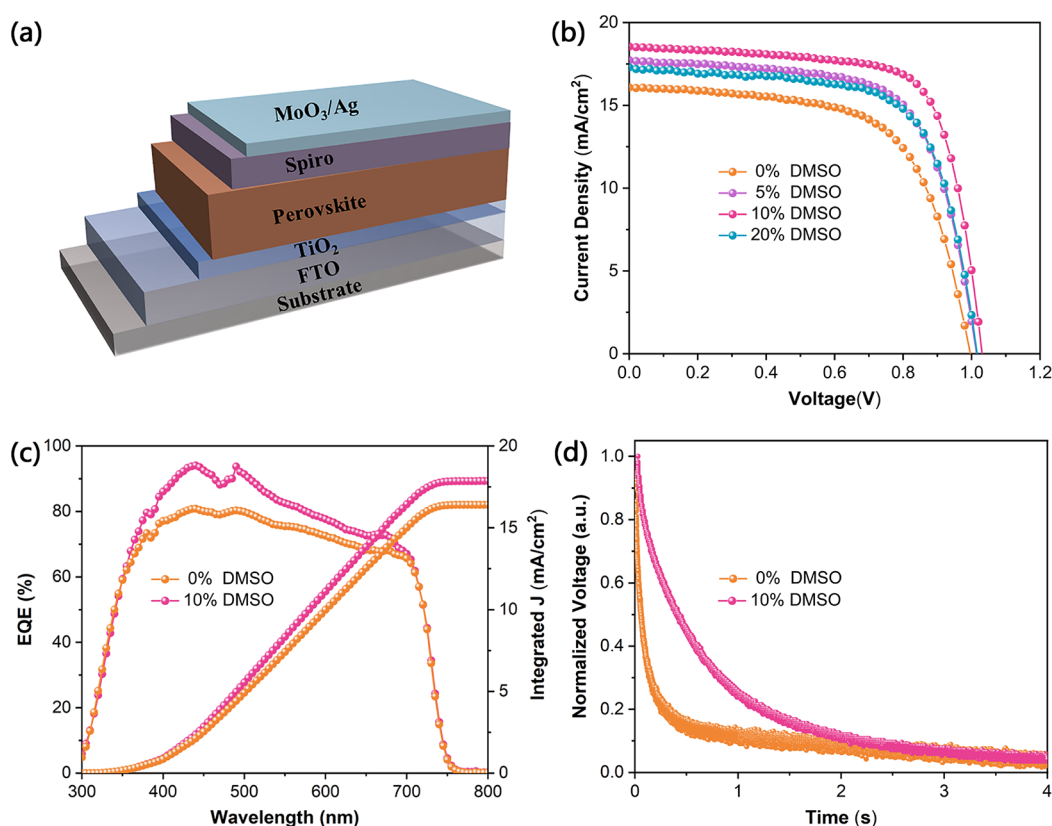**Figure 3.** Device performance of the $(PEA)_2(Cs)_4Pb_5I_{16}$-based PSCs: (a) schematic diagram of the device architecture, (b) $J-V$ characteristics in reverse scan with an area of 0.09 cm^2, (c) EQE and integrated J of the EQE curves, and (d) stable-state photovoltage attenuation curves.
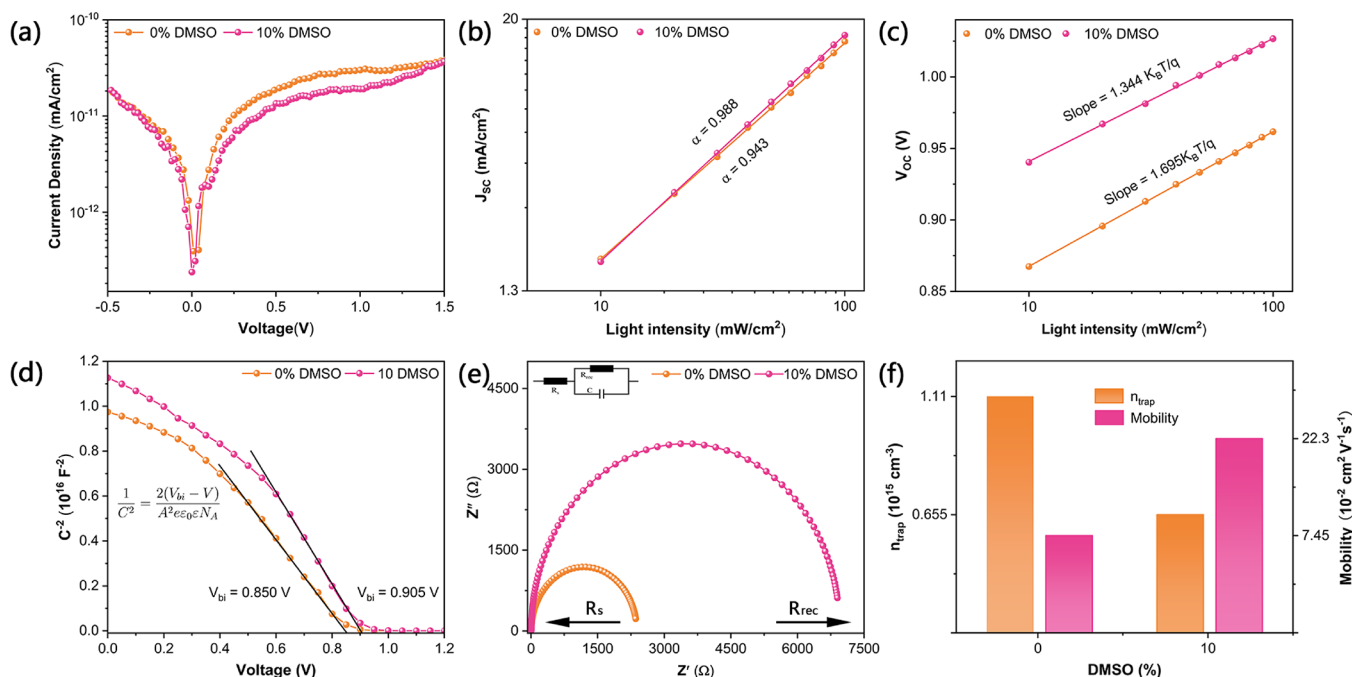

Figure 4. Electrical characteristics of the $(PEA)_2(Cs)_4Pb_5I_{16}$-based PSCs: (a) dark $J-V$ curves, (b) J_{SC} dependence on light intensity, (c) V_{OC} dependence on light intensity, (d) Mott−Schottky plots, (e) Nyquist plots, and (f) carrier mobility and trap density comparison of electron-only devices.

function, and corresponding fitting parameters are listed in Table S3. The optimized film exhibits a shorter lifetime τ_{ave} of 30.93 ns compared to the reference film (34.64 ns). Moreover, τ_2, representing a fast decay lifetime originated from the

quenching of carriers going through the interface, is also reduced for the optimized film (from 5.94 to 5.70 ns).[47] This result indicates that, in the optimized film, the carrier transfer and extraction are more effective due to the reduced trap-

mediated nonradiative recombination loss at the interface, which can lead to a positive influence on V_{OC}.[48]

The PSCs with the structure glass/FTO/compact-TiO$_2$/perovskite/Spiro-OMeTAD/MoO$_3$/Ag are fabricated to further investigate the impact of different solvent compositions in the 2D perovskite precursor on photovoltaic performance, as shown in Figure 3a. Figure 3b gives the photocurrent density–voltage ($J–V$) characteristics measured under standard AM 1.5G illumination at 100 mW/cm^2. The corresponding performance parameters are summarized in Table S4. The reference device shows a relatively inferior PCE of 10.11% with an open-circuit voltage (V_{OC}) of 0.99 V, a fill factor (FF) of 63.14%, and a short-circuit current density (J_{SC}) of 16.08 mA/cm^2. All devices with a DMSO additive show improved key parameters of PCE, V_{OC}, FF, and J_{SC}. The device with 10% DMSO exhibits a significantly improved PCE of 13.68% with a V_{OC} of 1.03 V, an FF of 71.54%, and a J_{SC} of 18.55 mA/cm^2. The increased V_{OC} can be attributed to the reduced nonradiative recombination loss, and the increased FF can be attributed to reduced trap density in the perovskite film.[37,48] The external quantum efficiency (EQE) and integrated J obtained from the EQE curves are shown in Figure 3c, and the optimized device exhibits an improved EQE between 360 and 700 nm compared with the reference device due to enhanced photon absorption.[49] A higher spectral response intensity indicates the more effective charge extraction capacity, leading to increased J_{SC}.[36] Meanwhile, the integrated J values of the reference and optimized devices are 17.85 and 16.40 mA/cm^2, respectively, which are well-consistent with the values obtained from the $J–V$ curves in Figure 3b. The stable-state photovoltage decay is measured, as shown in Figure 3d. The optimized device exhibits slower decay compared with the reference device, well indicating the reduced nonradiative recombination and increased V_{OC}.[50]

The dark $J–V$ curves of the reference and optimized devices are recorded in Figure 4a. It is clearly observed that the optimized device exhibits a lower dark current density compared with the reference device, suggesting a lower leakage current in the optimized device. The leakage current is mainly attributed to charge recombination, thus further indicating reduced charge recombination.[51] The $J–V$ characteristics were again measured under different incident light intensities ranging from 100 to 10 mW/cm^2 to further probe the charge carrier recombination kinetics. Figure 4b shows the relationship between J_{SC} and light intensity (I) on a double logarithmic scale, which follows the following equation: $J_{SC} \propto I^{\alpha}$. The slope ($\alpha = 0.988$) of the optimized device is closer to 1, while that of the reference device is 0.943. The less deviation from $\alpha \approx 1$ indicates lower bimolecular recombination at short circuit.[52] Thus, under short-circuit conditions, the optimized device shows less bimolecular recombination during carrier extraction and transport, leading to a higher J_{SC}.[51]

The relationship between V_{OC} and light intensity on a seminatural logarithmic scale is drawn in Figure 4c. Moreover, the dependence of V_{OC} on I is in accordance with the following equation: $V_{OC} = nKT/q(\ln(I))$, where n is an ideal factor related to recombination, K is the Boltzmann constant, T is temperature, and q is the electron charge.[53] The slopes of the reference and optimized devices are $1.695KT/q$ and $1.344KT/q$, respectively. The closer to $1kT/q$ the slope is, the lower the trap-assisted Shockley–Read–Hall recombination becomes, under open-circuit conditions.[51] Therefore, the optimized

device shows less trap-assisted Shockley–Read–Hall recombination under open-circuit conditions, leading to a higher V_{OC}.

Capacitance–voltage ($C–V$) measurements are performed to further investigate the influence of solvent composition on built-in potential (V_{bi}). Figure 4d shows $(1/C^2)–V$ curves of the reference and optimized devices, and the curves follow the Mott–Schottky equation: $1/C^2 = 2(V_{bi} - V)/A^2 e \varepsilon_0 \varepsilon N_A$, where V_{bi} represents the built-in potential, V represents the applied voltage, A represents the device area, N_A represents the carrier concentration, ε represents relative permittivity, and ε_0 represents vacuum permittivity.[54] The V_{bi} ($V_{bi} = 0.905$ V) of the optimized device is larger than that of the reference device ($V_{bi} = 0.850$ V). The relatively larger V_{bi} implies a stronger driving force for photogenerated carrier separation and an extended depletion region for suppressing carrier recombination.[54] Furthermore, electrochemical impedance spectroscopy (EIS) is employed to investigate the interfacial carrier recombination. The Nyquist plots and the equivalent circuit model are shown in Figure 4e. Compared with the reference device, the recombination resistance (R_{rec}) of the optimized device is significantly increased, while the series resistance (R_s) is reduced, indicating a reduced recombination loss, which can result in an improved V_{OC} and FF.[50,55]

The dark $J–V$ responses of electron-only devices (for the reference and optimized devices) are measured, as shown in Figure S5. The trap-state density (n_{trap}) can be obtained according to the following equation: $n_{trap} = 2\varepsilon_0 \varepsilon_r V_{TFL}/eL^2$, and the electron mobilities (μ) can be obtained from the Mott–Gurney law: $\mu = 8J_D L^3/9\varepsilon_0 \varepsilon_r V^2$, where ε_0 is the vacuum permittivity, ε_r is the relative dielectric constant, e is the elementary charge, L is the thickness of the perovskite film, and J_D is the dark current density.[36] The corresponding results are summarized in Figure 4f. The trap densities of the reference and optimized devices are 1.11×10^{15} and 6.55×10^{14} cm^{-3}, respectively. The calculated electron mobilities of the reference and optimized devices are 7.45×10^{-2} and 2.23×10^{-1} cm^2 V^{-1} s^{-1}, respectively. Obviously, the optimized device exhibits a relatively lower trap density and higher electron mobility, which is well supportive to improve the photovoltaic performance. To determine device reproducibility, photovoltaic parameters obtained from 20 cells are compared in Figure S6. Parameters of the optimized devices exhibit narrower distribution, which indicates good reproducibility. Lastly, the thermal stability of the device stored at 80 °C in N$_2$ and humidity stability with exposure to air with a humidity of 30–35% (for the reference and optimized devices) are tested, as shown in Figure S7. The optimized devices stored at 80 °C in N$_2$ maintain their initial PCE of approximately 74.58% after storage for 40 h, exhibiting better thermal stability compared to the reference devices (34.22%). Similarly, the optimized devices exposed to air with a humidity of 30–35% maintain their initial PCE of approximately 81.33% after storage for 40 h, exhibiting better humidity stability compared to the reference devices (52.56%). These results indicate that solvent engineering not only can improve efficiency but also improve stability.

■ CONCLUSIONS

In summary, the crystallization rate and crystal growth are demonstrated to be controllable via solvent engineering. The formation of a more stable intermediate phase will retard the crystallization rate, resulting in a longer time to form the final perovskite structure. Optimizing the solvent composition with

adding 10% DMSO in pure DMF leads to a high-quality $(PEA)_2(Cs)_4Pb_5I_{16}$ film with perfect coverage, increased film crystallinity, and a better vertical orientation to the substrate compared with the reference film. These improvements of film quality can optimize interface contact and reduce the nonradiative recombination loss, which is beneficial to charge transport/extraction between the ETL and perovskite. Hence, the optimized PSCs obtained a champion PCE of 13.68%.

■ ASSOCIATED CONTENT

Ⓢ Supporting Information

The Supporting Information is available free of charge at https://pubs.acs.org/doi/10.1021/acsaem.2c02345.

Experimental details; AFM and contact angle images; FWHM of the (111) and (202) planes; evolution of XRD patterns at different annealing time slots; real-time images at different annealing time slots during the crystallization process; dark $J-V$ measurements of the electron-only devices; statistical distribution of key photovoltaic parameters; thermal and humidity stability; peak intensities and corresponding intensity ratios ($I_{(202)}/I_{(111)}$) of the (111) and (202) planes; properties of solvents; key fitting parameters of TRPL; champion photovoltaic parameters (PDF)

■ AUTHOR INFORMATION

Corresponding Author

Qian Wang − School of Physical Science and Technology & National & Local Joint Engineering Laboratory for Optical Conversion Materials and Technology, Lanzhou University, Lanzhou 730000, China; ◉ orcid.org/0000-0003-2286-9164; Email: qianwang@lzu.edu.cn

Authors

Haiqiang Chen − School of Physical Science and Technology & National & Local Joint Engineering Laboratory for Optical Conversion Materials and Technology, Lanzhou University, Lanzhou 730000, China

Yutian Lei − School of Physical Science and Technology & National & Local Joint Engineering Laboratory for Optical Conversion Materials and Technology, Lanzhou University, Lanzhou 730000, China

Huanhuan Yao − School of Physical Science and Technology & National & Local Joint Engineering Laboratory for Optical Conversion Materials and Technology, Lanzhou University, Lanzhou 730000, China

Zhizai Li − School of Physical Science and Technology & National & Local Joint Engineering Laboratory for Optical Conversion Materials and Technology, Lanzhou University, Lanzhou 730000, China

Guoqiang Peng − School of Physical Science and Technology & National & Local Joint Engineering Laboratory for Optical Conversion Materials and Technology, Lanzhou University, Lanzhou 730000, China

Xufeng Zhou − School of Materials Science and Engineering, Liaocheng University, Liaocheng 252000, China

Haoxu Wang − Photovoltaic Materials and Devices Group, Delft University of Technology, 2628 CD Delft, the Netherlands; ◉ orcid.org/0000-0002-5430-0899

Zhiwen Jin − School of Physical Science and Technology & National & Local Joint Engineering Laboratory for Optical Conversion Materials and Technology, Lanzhou University, Lanzhou 730000, China; ◉ orcid.org/0000-0002-5256-9106

Complete contact information is available at:
https://pubs.acs.org/10.1021/acsaem.2c02345

Notes

The authors declare no competing financial interest.

■ ACKNOWLEDGMENTS

■ REFERENCES

(1) Chen, H.; Xiang, S.; Li, W.; Liu, H.; Zhu, L.; Yang, S. Inorganic Perovskite Solar Cells: A Rapidly Growing Field. Sol. RRL 2018, 2, 1700188.

(2) Wang, Y.; Zhang, T.; Xu, F.; Li, Y.; Zhao, Y. A Facile Low Temperature Fabrication of High Performance CsPbI$_2$Br All-Inorganic Perovskite Solar Cells. Sol. RRL 2018, 2, 1700180.

(3) Xiang, W.; Wang, Z.; Kubicki, D. J.; Tress, W.; Luo, J.; Prochowicz, D.; Akin, S.; Emsley, L.; Zhou, J.; Dietler, G.; et al. Europium-Doped CsPbI$_2$Br for Stable and Highly Efficient Inorganic Perovskite Solar Cells. Joule 2019, 3, 205−214.

(4) Wang, K.; Jin, Z.; Liang, L.; Bian, H.; Bai, D.; Wang, H.; Zhang, J.; Wang, Q.; Liu, S. All-Inorganic Cesium Lead Iodide Perovskite Solar Cells With Stabilized Efficiency Beyond 15%. Nat. Commun. 2018, 9, 4544.

(5) Ma, J.; Su, J.; Lin, Z.; He, J.; Zhou, L.; Li, T.; Zhang, J.; Liu, S.; Chang, J.; Hao, Y. Double Side Interfacial Optimization for Low-Temperature Stable CsPbI$_2$Br Perovskite Solar Cells with High Efficiency Beyond 16%. Energy Environ. Mater. 2022, 5, 637−644.

(6) Wang, P.; Zhang, X.; Zhou, Y.; Jiang, Q.; Ye, Q.; Chu, Z.; Li, X.; Yang, X.; Yin, Z.; You, J. Solvent-Controlled Growth of Inorganic Perovskite Films in Dry Environment for Efficient and Stable Solar Cells. Nat. Commun. 2018, 9, 2225.

(7) Ahmad, W.; Khan, J.; Niu, G.; Tang, J. Inorganic CsPbI$_3$ Perovskite-Based Solar Cells: A Choice for a Tandem Device. Sol. RRL 2017, 1, 1700048.

(8) Nam, J. K.; Chun, D. H.; Rhee, R. J. K.; Lee, J. H.; Park, J. H. Methodologies toward Efficient and Stable Cesium Lead Halide Perovskite-Based Solar Cells. Adv. Sci. 2018, 5, 1800509.

(9) He, J.; Su, J.; Di, J.; Lin, Z.; Zhang, S.; Ma, J.; Zhang, J.; Liu, S.; Chang, J.; Hao, Y. Surface Reconstruction Strategy Improves the All-Inorganic CsPbIBr$_2$ Based Perovskite Solar Cells and Photodetectors Performance. Nano Energy 2022, 94, No. 106960.

(10) Eperon, G. E.; Paternò, G. M.; Sutton, R. J.; Zampetti, A.; Haghighirad, A. A.; Cacialli, F.; Snaith, H. J. Inorganic Caesium Lead Iodide Perovskite Solar Cells. J. Mater. Chem. A 2015, 3, 19688−19695.

(11) Tan, S.; Yu, B.; Cui, Y.; Meng, F.; Huang, C.; Li, Y.; Chen, Z.; Wu, H.; Shi, J.; Luo, Y.; et al. Temperature-Reliable Low-Dimensional Perovskites Passivated Black-phase CsPbI$_3$ toward Stable and Efficient Photovoltaics. Angew. Chem., Int. Ed. 2022, 61, No. e202201300.

(12) Linxing, M.; Liang, L. Recent Research Progress on Operational Stability of Metal Oxide/Sulfide Photoanodes in Photoelectrochemical Cells. Nano Res. Energy 2022, DOI: 10.26599/NRE.2022.9120020.

(13) Lau, C. F. J.; Wang, Z.; Sakai, N.; Zheng, J.; Liao, C. H.; Green, M.; Huang, S.; Snaith, H. J.; Ho-Baillie, A. Fabrication of Efficient and Stable CsPbI$_3$ Perovskite Solar Cells through Cation Exchange Process. Adv. Energy Mater. 2019, 9, 1901685.

(14) Li, Z.; Zhou, F.; Wang, Q.; Ding, L.; Jin, Z. Approaches for Thermodynamically Stabilized CsPbI$_3$ Solar Cells. *Nano Energy* 2020, *71*, No. 104634.

(15) Swarnkar, A.; Marshall, A. R.; Sanehira, E. M.; Chernomordik, B. D.; Moore, D. T.; Christians, J. A.; Chakrabarti, T.; Luther, J. M. Quantum Dot-Induced Phase Stabilization of α-CsPbI$_3$ Perovskite for High-Efficiency Photovoltaics. *Science* 2016, *354*, 92−95.

(16) Jiang, Y.; Yuan, J.; Ni, Y.; Yang, J.; Wang, Y.; Jiu, T.; Yuan, M.; Chen, J. Reduced-Dimensional α-CsPbX$_3$ Perovskites for Efficient and Stable Photovoltaics. *Joule* 2018, *2*, 1356−1368.

(17) Wang, Y.; Zhang, T.; Kan, M.; Zhao, Y. Bifunctional Stabilization of All-Inorganic α-CsPbI$_3$ Perovskite for 17% Efficiency Photovoltaics. *J. Am. Chem. Soc.* 2018, *140*, 12345−12348.

(18) Liang, J.; Han, X.; Yang, J.-H.; Zhang, B.; Fang, Q.; Zhang, J.; Ai, Q.; Ogle, M. M.; Terlier, T.; Martí, A. A.; et al. Defect-Engineering-Enabled High-Efficiency All-Inorganic Perovskite Solar Cells. *Adv. Mater.* 2019, *31*, 1903448.

(19) Li, B.; Zhang, Y.; Fu, L.; Yu, T.; Zhou, S.; Zhang, L.; Yin, L. Surface Passivation Engineering Strategy to Fully-Inorganic Cubic CsPbI$_3$ Perovskites for High-Performance Solar Cells. *Nat. Commun.* 2018, *9*, 1076.

(20) Bo, L.; Zhen, L.; Xin, W.; Zonglong, Z. Interface Functionalization in Inverted Perovskite Solar Cells: From Material Perspective. *Nano Res. Energy* 2022, *1*, No. e9120011.

(21) Mao, L.; Stoumpos, C. C.; Kanatzidis, M. G. Two-Dimensional Hybrid Halide Perovskites: Principles and Promises. *J. Am. Chem. Soc.* 2019, *141*, 1171−1190.

(22) Shen, Y.; Liu, Y.; Ye, H.; Zheng, Y.; Wei, Q.; Xia, Y.; Chen, Y.; Zhao, K.; Huang, W.; Liu, S. Centimeter-Sized Single Crystal of Two-Dimensional Halide Perovskites Incorporating Straight-Chain Symmetric Diammonium Ion for X-Ray Detection. *Angew. Chem., Int. Ed.* 2020, *59*, 14896−14902.

(23) Lai, H.; Lu, D.; Xu, Z.; Zheng, N.; Xie, Z.; Liu, Y. Organic-Salt-Assisted Crystal Growth and Orientation of Quasi-2D Ruddlesden−Popper Perovskites for Solar Cells with Efficiency over 19%. *Adv. Mater.* 2020, *32*, 2001470.

(24) Lu, D.; Lv, G.; Xu, Z.; Dong, Y.; Ji, X.; Liu, Y. Thiophene-Based Two-Dimensional Dion−Jacobson Perovskite Solar Cells with over 15% Efficiency. *J. Am. Chem. Soc.* 2020, *142*, 11114−11122.

(25) Li, P.; Liu, X.; Zhang, Y.; Liang, C.; Chen, G.; Li, F.; Su, M.; Xing, G.; Tao, X.; Song, Y. Low-Dimensional Dion−Jacobson-Phase Lead-Free Perovskites for High-Performance Photovoltaics with Improved Stability. *Angew. Chem., Int. Ed.* 2020, *59*, 6909−6914.

(26) Nazarenko, O.; Kotyrba, M. R.; Wörle, M.; Cuervo-Reyes, E.; Yakunin, S.; Kovalenko, M. V. Luminescent and Photoconductive Layered Lead Halide Perovskite Compounds Comprising Mixtures of Cesium and Guanidinium Cations. *Inorg. Chem.* 2017, *56*, 11552−11564.

(27) Qi, W.; Wang, Y.; Wu, J.; Hu, Z.; Jia, C.; Zhang, H. Relaxor Ferroelectric and Photocatalytic Properties of BaBi$_4$Ti$_4$O$_{15}$. *Adv. Appl. Ceram.* 2019, *118*, 418−424.

(28) Liang, C.; Gu, H.; Xia, Y.; Wang, Z.; Liu, X.; Xia, J.; Zuo, S.; Hu, Y.; Gao, X.; Hui, W.; et al. Two-Dimensional Ruddlesden−Popper Layered Perovskite Solar Cells Based on Phase-Pure Thin Films. *Nat. Energy* 2021, *6*, 38−45.

(29) Fu, Y.; Zheng, W.; Wang, X.; Hautzinger, M. P.; Pan, D.; Dang, L.; Wright, J. C.; Pan, A.; Jin, S. Multicolor Heterostructures of Two-Dimensional Layered Halide Perovskites that Show Interlayer Energy Transfer. *J. Am. Chem. Soc.* 2018, *140*, 15675−15683.

(30) Mao, L.; Ke, W.; Pedesseau, L.; Wu, Y.; Katan, C.; Even, J.; Wasielewski, M. R.; Stoumpos, C. C.; Kanatzidis, M. G. Hybrid Dion−Jacobson 2D Lead Iodide Perovskites. *J. Am. Chem. Soc.* 2018, *140*, 3775−3783.

(31) Zhang, L.; Sun, C.; He, T.; Jiang, Y.; Wei, J.; Huang, Y.; Yuan, M. High-Performance Quasi-2D Perovskite Light-Emitting Diodes: from Materials to Devices. *Light: Sci. Appl.* 2021, *10*, 61.

(32) Zhang, J.; Zhang, L.; Li, X.; Zhu, X.; Yu, J.; Fan, K. Binary Solvent Engineering for High-Performance Two-Dimensional Perovskite Solar Cells. *ACS Sustainable Chem. Eng.* 2019, *7*, 3487−3495.

(33) Quan, L. N.; Yuan, M.; Comin, R.; Voznyy, O.; Beauregard, E. M.; Hoogland, S.; Buin, A.; Kirmani, A. R.; Zhao, K.; Amassian, A.; et al. Ligand-Stabilized Reduced-Dimensionality Perovskites. *J. Am. Chem. Soc.* 2016, *138*, 2649−2655.

(34) Gao, L.; Zhang, F.; Xiao, C.; Chen, X.; Larson, B. W.; Berry, J. J.; Zhu, K. Improving Charge Transport via Intermediate-Controlled Crystal Growth in 2D Perovskite Solar Cells. *Adv. Funct. Mater.* 2019, *29*, 1901652.

(35) Qiu, J.; Zheng, Y.; Xia, Y.; Chao, L.; Chen, Y.; Huang, W. Rapid Crystallization for Efficient 2D Ruddlesden−Popper (2DRP) Perovskite Solar Cells. *Adv. Funct. Mater.* 2019, *29*, 1806831.

(36) Yang, J.; Yang, T.; Liu, D.; Zhang, Y.; Luo, T.; Lu, J.; Fang, J.; Wen, J.; Deng, Z.; Liu, S.; Chen, L.; Zhao, K. Stable 2D Alternating Cation Perovskite Solar Cells with Power Conversion Efficiency >19% via Solvent Engineering. *Sol. RRL* 2021, *5*, 2100286.

(37) Yao, K.; Li, S.; Liu, Z.; Ying, Y.; Dvořák, P.; Fei, L.; Šikola, T.; Huang, H.; Nordlander, P.; Jen, A. K. Y.; et al. Plasmon-Induced Trap Filling at Grain Boundaries in Perovskite Solar Cells. *Light: Sci. Appl.* 2021, *10*, 219.

(38) Liu, P.; Han, N.; Wang, W.; Ran, R.; Zhou, W.; Shao, Z. High-Quality Ruddlesden−Popper Perovskite Film Formation for High-Performance Perovskite Solar Cells. *Adv. Mater.* 2021, *33*, 2002582.

(39) Zhou, L.; Su, J.; Lin, Z.; Guo, X.; Ma, J.; Li, T.; Zhang, J.; Chang, J.; Hao, Y. Synergistic Interface Layer Optimization and Surface Passivation with Fluorocarbon Molecules toward Efficient and Stable Inverted Planar Perovskite Solar Cells. *Research* 2021, *2021*, 9836752.

(40) Shan, S.; Li, Y.; Wu, H.; Chen, T.; Niu, B.; Zhang, Y.; Wang, D.; Kan, C.; Yu, X.; Zuo, L.; et al. Manipulating the Film Morphology Evolution toward Green Solvent-Processed Perovskite Solar Cells. *SusMat* 2021, *1*, 537−544.

(41) Jie, Z.; Leyu, B.; Yuanhang, C.; Baomin, X.; Alex, K.-Y. J. Self-Assembled Monolayer Enabling Improved Buried Interfaces in Blade-Coated Perovskite Solar Cells for High Efficiency and Stability. *Nano Res. Energy* 2022, *1*, No. e9120004.

(42) Fu, W.; Liu, H.; Shi, X.; Zuo, L.; Li, X.; Jen, A. K. Y. Tailoring the Functionality of Organic Spacer Cations for Efficient and Stable Quasi-2D Perovskite Solar Cells. *Adv. Funct. Mater.* 2019, *29*, 1900221.

(43) Lian, X.; Chen, J.; Zhang, Y.; Tian, S.; Qin, M.; Li, J.; Andersen, T. R.; Wu, G.; Lu, X.; Chen, H. Two-Dimensional Inverted Planar Perovskite Solar Cells with Efficiency over 15% via Solvent and Interface Engineering. *J. Mater. Chem. A* 2019, *7*, 18980−18986.

(44) Soe, C. M. M.; Nie, W.; Stoumpos, C. C.; Tsai, H.; Blancon, J.-C.; Liu, F.; Even, J.; Marks, T. J.; Mohite, A. D.; Kanatzidis, M. G. Understanding Film Formation Morphology and Orientation in High Member 2D Ruddlesden−Popper Perovskites for High-Efficiency Solar Cells. *Adv. Energy Mater.* 2018, *8*, 1700979.

(45) Chao, L.; Niu, T.; Gao, W.; Ran, C.; Song, L.; Chen, Y.; Huang, W. Solvent Engineering of the Precursor Solution toward Large-Area Production of Perovskite Solar Cells. *Adv. Mater.* 2021, *33*, 2005410.

(46) Fu, W.; Yan, J.; Zhang, Z.; Ye, T.; Liu, Y.; Wu, J.; Yao, J.; Li, C.-Z.; Li, H.; Chen, H. Controlled Crystallization of CH$_3$NH$_3$PbI$_3$ films for Perovskite Solar Cells by Various PbI$_2$(X) Complexes. *Sol. Energy Mater. Sol. Cells* 2016, *155*, 331−340.

(47) Yang, D.; Yang, R.; Wang, K.; Wu, C.; Zhu, X.; Feng, J.; Ren, X.; Fang, G.; Priya, S.; Liu, S. High Efficiency Planar-Type Perovskite Solar Cells with Negligible Hysteresis Using EDTA-Complexed SnO$_2$. *Nat. Commun.* 2018, *9*, 3239.

(48) Chen, Y.; Zuo, X.; He, Y.; Qian, F.; Zuo, S.; Zhang, Y.; Liang, L.; Chen, Z.; Zhao, K.; Liu, Z.; et al. Dual Passivation of Perovskite and SnO$_2$ for High-Efficiency MAPbI$_3$ Perovskite Solar Cells. *Adv. Sci.* 2021, *8*, 2001466.

(49) Shao, M.; Bie, T.; Yang, L.; Gao, Y.; Jin, X.; He, F.; Zheng, N.; Yu, Y.; Zhang, X. Over 21% Efficiency Stable 2D Perovskite Solar Cells. *Adv. Mater.* 2022, *34*, 2107211.

(50) He, J.; Su, J.; Lin, Z.; Ma, J.; Zhou, L.; Zhang, S.; Liu, S.; Chang, J.; Hao, Y. Enhanced Efficiency and Stability of All-Inorganic

CsPbI$_2$Br Perovskite Solar Cells by Organic and Ionic Mixed Passivation. *Adv. Sci.* **2021**, *8*, 2101367.

(51) Wang, X.; Ran, X.; Liu, X.; Gu, H.; Zuo, S.; Hui, W.; Lu, H.; Sun, B.; Gao, X.; Zhang, J.; et al. Tailoring Component Interaction for Air-Processed Efficient and Stable All-Inorganic Perovskite Photovoltaic. *Angew. Chem., Int. Ed.* **2020**, *59*, 13354−13361.

(52) Zheng, H.; Wu, W.; Xu, H.; Zheng, F.; Liu, G.; Pan, X.; Chen, Q. Self-Additive Low-Dimensional Ruddlesden−Popper Perovskite by the Incorporation of Glycine Hydrochloride for High-Performance and Stable Solar Cells. *Adv. Funct. Mater.* **2020**, *30*, 2000034.

(53) Wang, Y.; Wang, K.; Subhani, W. S.; Zhang, C.; Jiang, X.; Wang, S.; Bao, H.; Liu, L.; Wan, L.; Liu, S. Extrinsic Ion Distribution Induced Field Effect in CsPbIBr$_2$ Perovskite Solar Cells. *Small* **2020**, *16*, 1907283.

(54) Han, Y.; Zhao, H.; Duan, C.; Yang, S.; Yang, Z.; Liu, Z.; Liu, S. Controlled n-Doping in Air-Stable CsPbI$_2$Br Perovskite Solar Cells with a Record Efficiency of 16.79%. *Adv. Funct. Mater.* **2020**, *30*, 1909972.

(55) Fu, S.; Zhang, W.; Li, X.; Wan, L.; Wu, Y.; Chen, L.; Liu, X.; Fang, J. Dual-Protection Strategy for High-Efficiency and Stable CsPbI$_2$Br Inorganic Perovskite Solar Cells. *ACS Energy Lett.* **2020**, *5*, 676−684.